Theor Chem Account (2008) 119:489–500
DOI 10.1007/s00214-008-0410-2

REGULAR ARTICLE

Theoretical design of blue emitting materials based on symmetric and asymmetric spirosilabifluorene derivatives

Miao Sun · Ben Niu · Jingping Zhang

Received: 3 December 2007 / Accepted: 31 January 2008 / Published online: 16 February 2008

Abstract Equilibrium ground state geometry configurations and their relevant electronic properties of four experimentally reported asymmetric spirosilabifluorene derivatives are calculated by the HF(DFT)/6-31G(d) method. Their excited state geometries are investigated using the CIS/6-31G(d) method. The absorption and emission spectra are evaluated using the TD-B3LYP/6-31G(d) and TD-PBE0/6-31+G(d) levels both in gas phase and $CHCl_3$ solvent. Our results show an excellent agreement with the experimental data on their optical properties. To predict the substitution effect, the H/R (R = $–NO_2$, –CN, $–NH_2$ and $–OCH_3$) substituted symmetric and asymmetric spirosilabifluorene derivatives are also investigated, and the optical properties of H/R substituted derivatives are predicted in gas phase and $CHCl_3$ solvent. In comparison with the parent compound, significant red-shift is predicted for the emission spectra of the di-substituted symmetric derivatives with $–NH_2$ (96 nm), $–OCH_3$ (61 nm) and the push–pull (containing both $–NH_2$ and $–NO_2$) derivative (56 nm). It is found that the performance and the optical properties of these derivatives can be improved by adding push–pull substitutents. The largest change in the electronic and optical properties of this system can be obtained upon symmetric di-substitution among mono-, di-, tri- and tetra-substitutions.

Keywords Spirosilabifluorene · Electronic structure · Optical property · TD-DFT · Solvent effect

Electronic supplementary material The online version of this article (doi:10.1007/s00214-008-0410-2) contains supplementary material, which is available to authorized users.

M. Sun · B. Niu · J. Zhang (✉)
Faculty of Chemistry, Northeast Normal University,
Changchun 130024, China
e-mail: zhangjingping66@yahoo.com.cn

1 Introduction

Organic light-emitting diodes (OLEDs) have been the subjects of intensive investigation, since they were reported by Tang et al. [1]. The major challenges remain, including the need to develop a blue electroluminescent emitting material, which is essential for the development of a full color display based on the color changing medium technology or white emission [2–8].

Spirobifluorene derivatives have many kinds of applications such as in OLEDs [9–11], optically pumped solid-state laser [12], organic phototransistors [13], organic photovoltaic cells (OPVs) [14,15], nonlinear optical (NLO) materials [16], photochromic materials [17] and biology [18]. As a promising candidate for OLEDs, spirobifluorene exhibits superiority in various key domains, including blue-light-emitting devices with high efficiency and good color purity. OLEDs based on silole derivatives exhibit excellent performance with external electroluminescence quantum efficiencies close to the theoretical limit for a fluorescent material [19,20]. Compared with spirobifluorene, spirosilabifluorene may have an improved morphological stability in films [21–23]. Their polymers' optical and electronic properties such as UV absorption, electrochemical properties, photoluminescence (PL) and electroluminescence (EL) have been evaluated [24]. Spirosilabifluorene and its derivatives consist of two mutually perpendicular π-systems connected via a common sp^3-silicon atom, the so-called spiro-center. The "spiro" linked rigid backbone of these materials, via π–π-interaction, exhibits greater morphological stability and more intense fluorescence [25]. They have large electron affinities due to the σ^*–π^* conjugation arising from the interaction between the σ^* orbital of the two exocyclic Si–C bonds on the silole ring and the π^* orbital of the butadiene moiety [26–28]. This interaction leads to a large electron affinity,

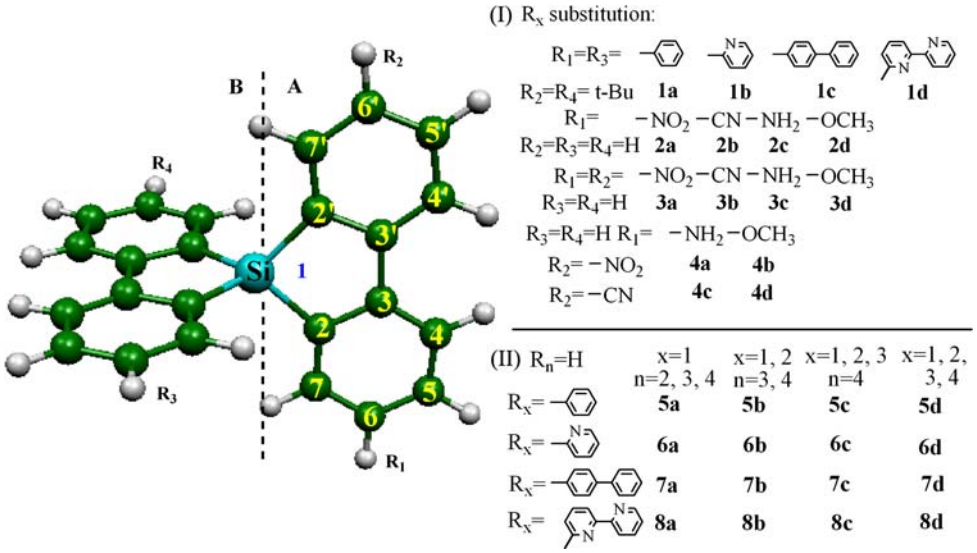

Fig. 1 Molecular structures of the investigated derivatives (*t*-Bu = *tert*-butyl)

i.e. high electron accepting capability and low lying lowest unoccupied molecular orbitals, which facilitates electron injection. Silole derivatives are believed to be excellent charge transport materials [29,30]. Spirobifluorenes have also been extensively studied as charge transport materials, and the frontier molecular orbitals give the main contribution to charge–transfer interactions [31,32]. However, the charge–transfer ability of spirosilafluorene is still under investigation [33].

Recently, a series of asymmetrically aryl-substituted 9,9′-spiro-9-silabifluorene derivatives, 2,2′-di-tert-butyl-7,7′-diphenyl-9,9′-spiro-9-silabifluorene (**1a**), 2,2′-di-tert-butyl-7,7′-dipyridin-2-yl-9,9′-spiro-9-silabifluorene (**1b**), 2,2′-di-tert-butyl-7,7′-dibiphenyl-4-yl-9,9′-spiro-9-silabifluorene (**1c**) and 2,2′-di-tert-butyl-7,7′-bis(2′,2″-bipyridin-6-yl)- 9,9′-spiro-9-silabifluorene (**1d**) were prepared by Lee et al [34]. The absorption spectrum of each of the novel spiro-linked silabifluorene was found to show a significant red shift relative to that of the corresponding carbon analogue. In addition, the corresponding solid-state films were reported to exhibit intense violet-blue emission (λ_{PL} = 398–415 nm).

Identifying the relation between the electronic properties and their geometrical structures of spirosilabifluorenes is important for the design of new electro-active/photo-active compounds and the tuning of their opto-electronic properties [35]. Although this task can be addressed from the theoretical standpoint, a few computational studies relating to this type of materials can be found in the literature [36]. To the best of our knowledge, no theoretical investigation of the four derivatives has been reported so far to explain the similar emission spectra of different substituents. In this contribution, we investigated the optical and electronic properties of asymmetric spirosilabifluorene derivatives (**1a**–**1d**) with the aim to get an in-depth explanation of the experimental results, and to design new photoluminescent materials based on the spirosilabifluorene moiety. One of the most important electro-active and photo-active materials is functionalized by electron-donating and electron-accepting groups through a π-conjugated linker. The molecules with push–pull structures have attracted much academic and technological research interest [37–43]. It is meaningful to design new push–pull system and to probe the optical properties of spirosilabifluorene-based materials. Thus, taking spirosilabifluorene (SSF) as parent compound, H/R (R = –NO_2, –CN, –NH_2 and –OCH_3) substituted SSF derivatives are investigated. In addition, it is also an efficient approach of improving the performance and tuning the optical properties of these derivatives. Herein, we report our computational results, with special attention to the structures, the HOMO–LUMO gaps, charge transfer, and the absorption/emission spectra.

2 Computational details

The structures of two series of spirosilabifluorene derivatives (**1a**–**8d**) considered in this work are shown in Fig. 1. Two groups of compounds have been considered in our computational work. The first corresponds to the H/R (R = –NO_2, –CN, –NH_2, and –OCH_3) substituted SSF derivatives on position 6 and/or 6′ (***n*a**–***n*d**, n = 2–4, Fig. 1I): **2a–2d** (mono-substituted asymmetric derivatives with R_1 = –NO_2, –CN, –NH_2, –OCH_3, R_2 = R_3 = R_4 = H), **3a–3d** (di-substituted symmetric derivatives with R_1 = R_2 = –NO_2, –CN, –NH_2, –OCH_3, R_3 = R_4 = H) and **4a–4d** (di-substituted push–pull systems with R_1 = –NO_2, –CN, R_2 = –NH_2, –OCH_3, R_3 = R_4 = H). The other series of derivatives are obtained by a systematic substitution of symmetric and asymmetric mono-, di-, tri- and tetra-substituted phenyl,

biphenyl, pyridyl, and bipyridyl derivatives. They are shown in Fig. 1II (***n*a**–***n*d**, $n = 5$–8, where R_x denotes aryl rings, R_n denotes hydrogen).

All the geometry optimizations for the ground state (S_0) were performed using the ab initio Hartree Fock (HF) with the 6-31G(d) [44–47] split valence plus polarization basis set, and the density functional theory (DFT)-B3LYP [48–50] method for some model compounds as well. B3LYP/6-31G(d) single point energy calculation was used to study the electronic properties in S_0. The low-lying excited-state (S_1) structures were optimized using the configuration interaction with single excitations (CIS) [51] method and 6-31G(d) basis set. The optical spectra were calculated using the TD-B3LYP [52] with the 6-31G(d) basis set to obtain estimates including some account of electron correlation. For comparison with the experimental results, the CIS, ZINDO [53], TD-PBE0 [54] /6-31G(d) and TD-PBE0/6-31+G(d) [55] levels were also employed in optical spectra calculations. Based on the optimized structures in gas phase, we performed the polarized continuum model (PCM) [56,57] calculations at the TD-DFT level to give a comparison of the optical spectra in gas phase and in the $CHCl_3$ solvent (in both equilibrium [58] and non-equilibrium solvation). Two common density functionals with different fractions of orbital exchange, namely BHandHLYP [59] (50%) and B3LYP (20%), were used in predicting the charge transfer states. All the computational results were performed using the Gaussian 03 package [60]. Gaussview [61] and Molekel [62] softwares are used to manipulate the molecular orbitals and structures, respectively.

3 Results and discussions

3.1 Comparison of computational methods, electronic and optical properties for 1a–1d

3.1.1 Geometries of ground states

More detailed insights into the nature of the excited states responsible for the optical properties can be gained by looking at the frontier molecular orbitals (FMOs), when calculated on a reliable geometry of a molecule. The optimized geometrical parameters for **1a**–**1d** at the HF and B3LYP levels using the 6-31G(d) basis set are listed in Table S1 in Supporting Information. The optimized structures show that the bond lengths and bond angles are slightly method dependent. The largest difference for the bond length is found in C_2–C_3 and C_2'–C_3', with the HF values being 0.013–0.015 Å shorter than the B3LYP ones. Moreover, when comparing the bond length of C_3–C_3', the results at the HF level are 0.006–0.007 Å larger than those at the B3LYP level. The difference of the bond lengths between the single bonds (C_2–C_3, C_2'–C_3') and double bonds (C_3–C_3') is ca. 0.088 Å at the HF level and ca. 0.067 Å at the B3LYP level, and the difference between these two methods is ca. 0.021 Å. The other variations in bond length are all less than 0.01 Å. The difference in bond angles and dihedral angles within the silafluorene parts are less than 1°, and these derivatives keep their mutually perpendicular π-systems. The major differences are found in the dihedral angles between substituents and the silafluorene parts. The dihedral angles between silafluorene part and the phenyl/pyridyl substituents are 44°/26° (**1a/1b**) at the HF level, and 37°/17° (**1a/1b**) at the B3LYP level. It indicates that the hydrogen-free pyridyl ring twists less than the phenyl group. Note that the lowest energy conformer for bipyridyl corresponds to that with the nitrogen atoms in a *trans*-conformation. The dihedral angles between the outer and the inner aryl rings for biphenyl and bipyridyl substituents are −45° (**1c**) and 4° (**1d**) at the HF level, −37° (**1c**) and 3° (**1d**) at the B3LYP level. Therefore, the twisting for the backbone in **1b** and **1d** are reduced compared with **1a** and **1c**.

3.1.2 Electronic structure and absorption spectra

To investigate the effect of electron correlation on the computed energies and spectra, calculations using the TD-B3LYP, TD-PBE0, CIS, and ZINDO methods, were carried out based on both the HF/6-31G(d) and B3LYP/6-31G(d) optimized S_0 geometries. For the sake of comparison, and to estimate the accuracy of the theoretical level applied in this work, we list both the experimental [33] and theoretical [35] maximum absorption wavelengths (λ_{abs}) for **1a**–**1d** in Table 1 (the results at the ZINDO, CIS/6-31G(d) levels and the absorption spectra based on B3LYP optimized geometries are shown in Table S2 in Supporting Information). The calculated λ_{abs} values [TD-B3LYP/6-31G(d), TD-PBE0/6-31G(d), and TD-PBE0/6-31+G(d)] based on the HF/6-31G(d) geometries are all in excellent agreement with experimental results [34], with the maximum deviation being less than 7 nm. The results at the TD-B3LYP/6-31G(d) and TD-PBE0/6-31G(d) level are only 5–7 nm longer and 2–6 nm shorter than the experimental results, respectively. The results at the PBE0/6-31+G(d) level are shorter (longer) than the experimental measurement for **1a** (**1b** and **1c**). These results give credit to the computational approach, and appropriate optical spectra may be predicted at these levels for the spirosilabifluorene derivatives, which can be applied for the systems under investigation. Our results indicate that λ_{abs} do not change significantly in **1a**–**1d** (within the range of 8 nm at the TD-B3LYP/6-31G(d) level, and 7 nm at the TD-PBE0/6-31+G(d) level), only a slight blue shift being found in **1a**.

Since the relative ordering of the occupied and unoccupied orbitals provides a reasonable qualitative indication of the excitation properties, it is useful to examine the frontier molecular orbitals (FMOs) of the derivatives [63]. The

Table 1 The computed maximum absorption (λ_{abs}), oscillator strength (f), main CI expansion and coefficients in gas phase

	Calc[a]	f[a]	Main CI expansion/coefficients	Exp[b]	Calc[c]	f[c]	Calc[d]	f[d]	Calc[e]
1a	314	0.200	H → L (0.65)	307	305	0.278	310	0.259	294
1b	322	0.221	H → L (0.67)	317	311	0.416	313	0.426	309
1c	320	0.420	H → L (0.64)	315	310	0.638	312	0.608	303
1d	322	0.267	H → L (0.66)	–	313	0.458	317	0.458	319

H HOMO, *L* LUMO
[a] TD-B3LYP//HF/6-31G(d)
[b] Experimental data from Ref. [34]
[c] TD-PBE0//HF/6-31G(d)
[d] TD-PBE0/6-31+G(d)//HF/ 6-31G(d)
[e] Theoretical results from Ref. [36]

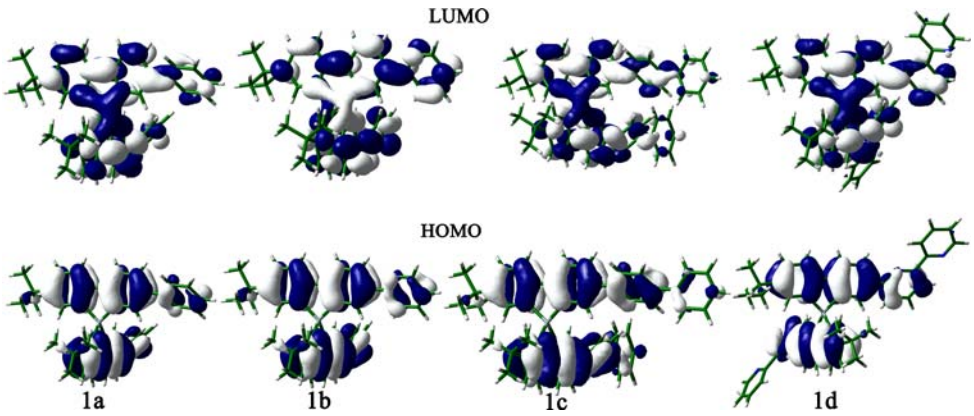

Fig. 2 B3LYP//HF/6-31G(d) electron density contours of the orbitals involved in the transitions for **1a**–**1d**

electron density contours of the highest occupied molecular orbitals (HOMOs) and the lowest unoccupied molecular orbitals (LUMOs) for **1a**–**1d** are shown in Fig. 2. A careful analysis of the FMOs for **1a**–**1d** indicates that they are mainly distributed on the silafluorene parts and their adjacent aryl rings, the external aryl rings have little (**1c**) or no contribution (**1d**). The silicon atom definitely has some contribution to the LUMO, while no contribution to the HOMO was observed from it. The HOMO energy (E_{HOMO}) of **1c** is slightly higher (−5.42 eV) than those for **1a** (−5.47 eV), **1b** (−5.52 eV) and **1d** (−5.54eV), due to the small amount of the orbital contribution on the external phenyl ring. The LUMO energy (E_{LUMO}) of **1b** (−1.39 eV) and **1d** (−1.40 eV) are similar, and stabilized comparatively to those for **1a** (−1.20 eV) and**1c** (−1.31 eV). The stabilized E_{LUMO} for **1b** and **1d** can be ascribed to the more planar structures of the pyridyl and bipyridyl rings (as mentioned in Sect. 3.1.1), which favor the stronger bonding orbitals between silafluorene parts and their adjacent pyridyl or bipyridyl rings than those of phenyl and biphenyl substituents, as well as the introduction of N atoms. Both the similar FMO distribution patterns and similar energy gap (Eg) values between HOMOs and LUMOs for **1a**–**1d** (4.27, 4.13, 4.11, and 4.14 eV) are responsible for their similar absorption properties, and the slightly larger Eg for **1a** results in the small blue shift compared with **1b**–**1d**.

3.1.3 Excited state structures

Studies of the excited state properties for a number of molecules using the CIS method have found that despite the tendency of CIS to overestimate electronic transition energies, the excited state potential energy surface can often be quite accurate [64–68]. Thus, the CIS/6-31G(d) was used to get the excited state structures for **1a**–**1d**. Comparing with the structures in S_0, some of the bonds in S_1 equilibrium geometries are lengthened, some others being shortened. All of the significant changes are located on one of the two (A or B) fragments, the other one remaining practically unaffected. The C_3–C_3', C_4–C_5, C_4'–C_5' and C_6–C_{R1} bonds are shortened upon excitation, the C_2–C_3, C_2'–C_3', C_3–C_4, C_3'–C_4', C_5–C_6 and C_5'–C_6' ones being lengthened. The central silole ring is revealed to be the most distorted with the C_2–C_3 and C_2'–C_3' bond lengths (which are predicted in the range of 1.45–1.47 Å), being lengthened by ca 0.06 Å upon excitation. The optimized C_3–C_3' bond lengths in the range from 1.40 to 1.41 Å, are found to be shortened by ca 0.09 Å compared with their corresponding S_0. One of the dihedral angles between the silafluorene part and the phenyl/biphenyl rings decreases by ca 25° for **1a** and **1c** in S_1. According to the very small dihedral angles (≤1°) between the ortho-hydrogen-free pyridyl and the silafluorene parts for **1b** and **1d** in S_1,

Table 2 Computed maximum emission (λ_{em}), oscillator strength (f), main CI expansion and coefficients in gas phase

	Calc[a]	f[a]	Main CI expansion/coefficients	Exp[b]	Calc[c]	f[c]	Calc[d]	f[d]
1a	385	0.473	H ← L (0.65)	383	376	0.493	380	0.488
1b	387	0.585	H ← L (0.64)	382	378	0.613	385	0.617
1c	397	0.939	H ← L (0.67)	393	386	0.965	391	0.96
1d	389	0.658	H ← L (0.69)	–	380	0.684	386	0.675

[a] The values at B3LYP//CIS/6-31G(d)
[b] Experimental data from Ref. [34]
[c] The values at PBE0//CIS/6-31G(d)
[d] The values at PBE0/6-31+G(d)//CIS/6-31G(d)

effectively coplanar configuration allows a better π orbital overlap. Moreover, these molecules maintain their two mutually perpendicular π-systems in S_1 also. Due to the singlet excited state corresponding to an excitation from the HOMO to the LUMO, we can give a good explanation of the bond length variation by analyzing the FMOs. The HOMO are antibonding in C_3–C_3', C_4–C_5, C_4'–C_5' and C_6–C_{R1}, while the LUMO are bonding in these regions. Therefore, these bonds are shorter in S_1. The LUMO is antibonding in C_2–$C_3'C_2'$–C_3', C_3–C_4, C_3'–C_4', C_5–C_6 and C_5'–C_6', while the HOMO is bonding. These bonds are hence longer in S_1.

3.1.4 Emission properties

The emission spectra were predicted at the TD-B3LYP/6-31G(d), TD-PBE0/6-31G(d), and TD-PBE0/6-31+G(d) level. We summarize the calculation results of the emission wavelength (λ_{em}) with the corresponding oscillator strengths in Table 2. These results at the TD-PBE0/6-31G(d) level are 4–7 nm blue-shifted from the experimental results, while those at both the TD-B3LYP/6-31G(d) and TD-PBE0/6-31+G(d) levels show a good agreement with the experimental results, the maximum deviation being of only 5 nm. Moreover, one can find from Table 2 that the results at the TD-B3LYP/6-31G(d) and TD-PBE0/6-31+G(d) levels are quite similar, the difference between these two methods being 5 nm for **1a**, 2 nm for **1b** and 6 nm for **1c**. Thus, one may figure out that both the TD-B3LYP/6-31G(d) and TD-PBE0/6-31+G(d) levels can predict reliable optical results for spirosilabifluorene derivatives under investigation. According to our results, the calculated λ_{em} value of **1c** (at both these two methods) is red-shifted comparing with **1a**, **1b** and **1d**, and its corresponding f is twice larger than the others. This is in excellent agreement with the experimental foundings that **1c** shows intense violet–blue emissions [34]. This may be due to the efficient conjugation from the external phenyl group in S_1 by decreasing the torsional angle between the silafluorene part and the phenyl ring, corresponding to some amount of orbital distribution on the external ring (see Figure S1 in Supporting Information). On the other hand, the pyridyl and bipyridyl parts in **1b** and **1d** have no significant influence on λ_{em} as compared with **1a**, this is consistent with the FMO distribution patterns in S_1, where the shape of the FMOs are nearly identical, and only distributed on the silafluorene part and adjacent aryl ring. No significant contribution is found for the external pyridyl ring.

3.1.5 Solvent effect and Stokes shift

On the basis of the optimized structures (S_0 and S_1), we predicted the optical spectra for **1a**,**1b**, and **1c** in $CHCl_3$ solvent taking into account both non-equilibrium and equilibrium solute–solvent effects at two reliable theoretical levels (PCM-TD-B3LYP/6-31G(d) and PCM-TD-PBE0/6-31+G(d)). The introduction of the solvent effects (PCM model) in the TD-DFT calculations leads to a slight red-shift for the λ_{em} values, which was estimated to be 6–7 nm in non-equilibrium solvation and 10–14 nm in equilibrium solvation compared with the values in gas phase, the difference between non-equilibrium and equilibrium results being less than 7 nm within these two methods. One can find that there is no drastic displacement of λ_{em} when solvent effects are taken into account, while the oscillator strength is slightly increased. Therefore, it is reasonable to conclude that no distinct solvent effect in these weakly polar molecules can be expected. As PCM calculation is highly time consuming for such large molecules, the emission spectra of **1c** failed to obtain at the TD-PBE0/6-31+G(d) level. According to our PCM-TD-B3LYP results calculated on **1a**–**1c**, the Stokes shifts in non-equilibrium $CHCl_3$ solvent are 76, 71 and 82 nm, respectively, whereas the PCM-TD-PBE0 results are 77 nm (**1a**) and 74 nm (**1b**), slightly deviating the experimental Stokes shifts of 76 nm (**1a**), 65 nm (**1b**) and 78 nm (**1c**). The Stokes shifts in equilibrium solvation show larger deviations from the experimental results, and the calculated Stokes shifts at the PCM-TD-B3LYP/6-31G(d) level agree very well with the available experimental results (Table 3).

Table 3 Computed maximum wavelength (λ_{abs} and λ_{em}), oscillator strength (f), the difference between non-equilibrium and equilibrium ($\Delta\lambda$) and the Stokes shift (S) in $CHCl_3$ solvent

	B3LYP/6-31G(d)							PBE0/6-31+G(d)							
	Non-equilibrium			Equilibrium				Non-equilibriumm			Equilibrium				
	λ	f	S	λ	f	S	Δλ	λ	f	S	λ	f	S	Δλ	Exp[a]
Absorption															
1a	315	0.32		317	0.43		2	311	0.38		312	0.5		1	
1b	323	0.43		325	0.62		2	319	0.62		321	0.78		3	
1c	322	0.65		323	0.52		1	–	–		–	–			
Emission															
1a	391	0.62	76	395	0.74	79	4	388	0.65	77	393	0.78	81	5	76
1b	394	0.76	71	401	0.9	74	7	393	0.8	74	398	0.95	77	5	65
1c	404	1.15	82	411	1.29	88	7	–	–	–	–	–	–		78

[a] Experimental data from Ref. [34]

3.2 Optimized geometries of S_0 and S_1 states for the H/R substituted derivatives

On the basis of the reliable methods, we design some new blue emitting materials by substituting H by $–NO_2$, –CN, $–NH_2$, and $–OCH_3$. Since no such kinds of derivatives were reported yet, we compared the substituted derivatives to the parent compound SSF in order to understand the substitution effect in a better way. In general, the comparison of the optimization results for SSF and its derivatives in S_0 does not reveal any significant change on the geometry of the skeleton. Within the H/R substituted derivatives, no more than 0.008 Å of variation is predicted in bond lengths, whereas the predicted variation in bond angles is found in the range of 0.01–3.01° for the SSF skeleton. The structural relaxation upon $S_0 \rightarrow S_1$ transition is mainly localized on A fragment, which contains the electron-accepting and electron-donating groups, the other one remaining practically unaffected. However, the $S_0 \rightarrow S_1$ structural changes in **2b**, which contains one –CN substituent, are mainly localized on B fragment. This maybe implicate that the mono-substitution with –CN does not induce any significant contribution to the transitions. In general, the central silole ring is revealed to be the most distorted with the C_2–C_3 and C_2'–C_3' bond lengths (which are predicted in the range of 1.457–1.472 Å), being lengthened by 0.05–0.06 Å upon excitation. The optimized C_3–C_3' bond lengths in the range from 1.402 to 1.406 Å, are found to be shortened by 0.08–0.09 Å compared with their corresponding values in S_0.

3.3 Electronic structure for H/R substituted derivatives

In Fig. 3, we give the electron density contours of the FMOs (HOMO−1, HOMO, LUMO, LUMO+1) for **SSF**, **2a**, **3a** and **4a** as representatives of the system under investigation

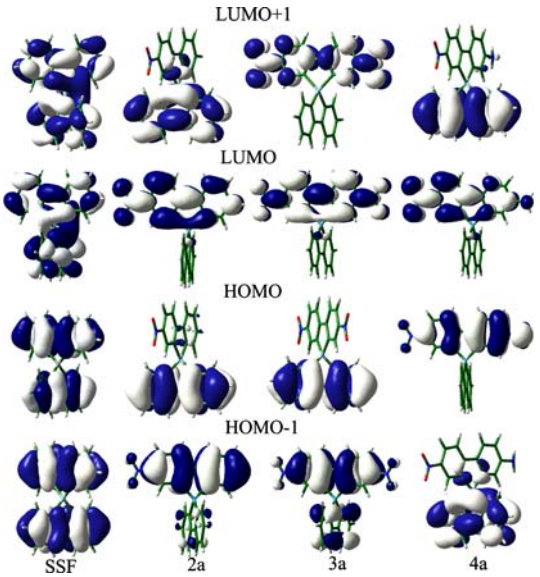

Fig. 3 B3LYP//HF/6-31G(d) electron density contours of the orbitals involved in transitions for SSF, **2a**, **3a** and **4a**

(see also Figures S2 in Supporting Information). One may figure out that for **1a**–**1d**, both the structural variation upon $S_0 \rightarrow S_1$ transition and the FMOs in S_1 are mainly localized on one of the silafluorene parts, as reported in Sects. 3.1.2 and 3.1.3. Thus we considered the H/R mono-, symmetric di-substitution and push–pull substitutions on one fragment. All of these FMOs spread over the π-conjugated backbone as **1a**–**1d**. They are, respectively, antibonding and bonding between the carbon atoms bridging the two phenyl groups within the silafluorene part for the HOMO−1, HOMO, LUMO and LUMO+1. The same bonding–antibonding pattern is also observed between adjacent atoms in the same aryl ring. Upon excitation, one electron from the HOMO or HOMO−1 can be expected to move to the LUMO or LUMO+1, bonds

showing a HOMO/HOMO−1 bonding pattern are lengthened, those showing a HOMO/HOMO−1 antibonding pattern being shortened in S_0. This is in agreement with the structural changes discussed in Sects. 3.1.3 and 3.2. For the parent compound SSF, it can be seen from Fig. 3 that all these FMOs are localized on the whole molecule, and its HOMO−1 and HOMO, LUMO and LUMO+1 look the same. However, within the H/R substituted derivatives, the FMOs are found to be localized on one of the silafluorene parts, except for **3a** whose HOMO−1 is localized on the whole molecule. It can be concluded from Fig. 3 that within the electron-accepting substituted derivatives (**2a**, **2b**, **3a**, **3b**), the HOMO−1 and LUMO are mainly localized on A fragment, while the HOMO and LUMO+1 are mainly localized on B fragment without substituents, except for the LUMO+1 orbital of the di-substituted **3a** and **3b** (Fig. 3 and S2 in Supporting Information). For the derivatives with electron-donating substituents (**2c**, **2d**, **3c**, **3d**), the HOMO−1 and LUMO are mainly localized on B fragment, while the HOMO and LUMO+1 are localized on A fragment. According to the result of the push–pull system (**4a**–**4d**), we can find that all the HOMO and LUMO spread over A fragment, the electron-accepting and electron-donating substituents, while all the HOMO−1 and LUMO+1 spread over the other fragment of B.

For a better understanding of the influence of the H/R substitutions on the E_{FMOs}, Fig. 4 shows the evolution of the computed energies for the first three HOMOs and LUMOs in S_0 (Table S3 in Supporting Information). The electron-acceptor capacity of $-NO_2$ and –CN results in the decrease of both the E_{HOMOs} and E_{LUMOs} in **2a/b** and **3a/b**, while the E_{LUMOs} values are more affected than E_{HOMOs}. However, E_{HOMOs} and E_{LUMOs} increase for **2c/d** and **3c/d**, due to the effect of electron-donor capacity of $-NH_2$ and $-OCH_3$, especially in the symmetric di-substitution cases (**3c**, **3d**). Within these derivatives (**2c/d** and **3c/d**), E_{HOMOs} are more lifted, while their E_{LUMOs} are close to that of **SSF**. For **4a**, **4b**, **4c** and **4d**, which possess push–pull substituents on one fragment of **SSF**, the E_{HOMOs} increase while the E_{LUMOs} decrease. Their E_g values become much smaller compared with pure electron-accepting or electron-donating substituented derivatives. As we can see from the figure, the energies of these orbitals are obviously changed by adding different electron-accepting and electron-donating substituents. Thus, adding different electron-accepting and electron-donating substituents can be an efficient way of tuning the E_{FMOs} of these derivatives.

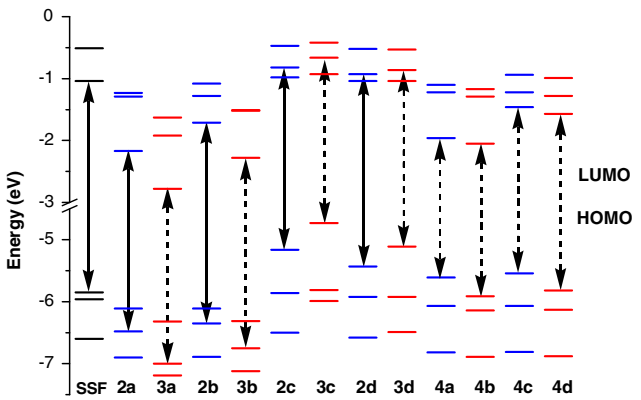

Fig. 4 Evolution of the B3LYP//HF/6-31G(d) computed energies for the six FMOs in H/R substituted derivatives (the *arrows* point to the orbitals involved in the transitions, the *dotted arrows* are used for the di-substituted including push–pull derivatives, and line arrows for SSF and its mono- substituted derivatives)

The FMOs of the H/R substituted derivatives in S_1 at the TD-B3LYP//CIS/6-31G(d) level (see Figure S3 in Supporting Information) are localized on one of the silafluorene parts, which have similar bonding–antibonding pattern to those of **1a**–**1d**, except for **2a** whose orbitals are localized on the whole molecule. The orbitals involved in the transitions show the same bonding–antibonding pattern as they are in S_0. Within these derivatives, most of these orbitals are HOMOs and LUMOs, except for **3a** (LUMO→HOMO−1). According to the energy considerations, the E_{HOMO} are more increased, while the E_{LUMO} are more decreased in S_1 than they are in S_0 (see details in Figure S4 and Table S3 in Supporting Information). As a net effect, the E_g values become smaller, and the same tendency is also found for both S_1 and S_0 within the rest of the derivatives.

3.4 Optical properties for H/R substituted derivatives

3.4.1 Absorption spectra

In Table 4 we list the calculated λ_{abs}, the oscillator strength (f), and the main CI expansion of the derivatives of interest on the basis of the TD-B3LYP/6-31G(d) level [the results at the TD-PBE0/6-31+G(d) level are listed in Table S4 in Supporting Information]. For the derivatives with electron-accepting or electron-donating substituents, excitation to the S_1 state is weakly allowed, whereas the $S_0 \rightarrow S_2$ electronic transition possesses a larger f. Moreover, the transition corresponds to a HOMO−1→LUMO excitation in **2a/b** and **3a/b**, while for **2c/d** and **3c/d**, it corresponds to a HOMO→LUMO+1 excitation. Only the derivatives with push–pull substituents (**4a**–**4d**) possess larger f for $S_0 \rightarrow S_1$ transition. Within the H/R substituted derivatives, the calculated λ_{abs} values reveal a red shift of the absorption spectra compared to **SSF**. One may find that the red shift ($\Delta\lambda_{abs}$) increases for the mono- and di-substituted derivatives in the order of $-CN < -NO_2 < -OCH_3 < -NH_2$, while for the derivatives with push–pull substituents on one fragment of SSF, the increasing order is **4d** < **4c** < **4b** < **4a**. The calculated spectral features depend on the change of the E_g values and the E_{FMOs} described above. According to Fig. 4, smaller

Table 4 TD-B3LYP/6-31G(d) and PCM-B3LYP/6-31G(d) computed wavelengths (λ_{abs} and λ_{em}), oscillator strengths, transitions assignment and coefficients of H/R substituted derivatives

	λ^a (nm)	f^a	Transitions	Main CI expansion/coefficient	λ^b (nm)	f^b
Absorption						
SSF	296	0.035	$S_0 \rightarrow S_1$	H → L (0.65)	297	0.061
2a	317	0.294	$S_0 \rightarrow S_2$	H−1→L (0.65)	336	0.419
2b	299	0.169	$S_0 \rightarrow S_2$	H−1→L (0.61)	303	0.311
2c	331	0.053	$S_0 \rightarrow S_2$	H → L + 1 (0.65)	337	0.084
2d	319	0.056	$S_0 \rightarrow S_2$	H → L + 1 (0.66)	320	0.083
3a	328	0.147	$S_0 \rightarrow S_2$	H−1→L (0.65)	342	0.237
3b	306	0.322	$S_0 \rightarrow S_2$	H−1→L (0.62)	309	0.5
3c	357	0.036	$S_0 \rightarrow S_2$	H → L + 1 (0.70)	362	0.055
3d	340	0.048	$S_0 \rightarrow S_2$	H → L + 1 (0.66)	340	0.065
4a	371	0.358	$S_0 \rightarrow S_1$	H → L (0.65)	411	0.482
4b	356	0.297	$S_0 \rightarrow S_1$	H → L (0.65)	379	0.381
4c	343	0.191	$S_0 \rightarrow S_1$	H → L (0.62)	356	0.358
4d	330	0.190	$S_0 \rightarrow S_1$	H → L (0.64)	335	0.318
Emission						
SSF	360	0.099	$S_1 \rightarrow S_0$	H ← L (0.64)	363	0.147
2a	393	0.038	$S_1 \rightarrow S_0$	H ← L (0.61)	411	0.066
2b	364	0.098	$S_1 \rightarrow S_0$	H ← L (0.64)	367	0.145
2c	408	0.106	$S_1 \rightarrow S_0$	H ← L (0.64)	420	0.158
2d	391	0.112	$S_1 \rightarrow S_0$	H ← L (0.64)	393	0.158
3a	378	0.391	$S_2 \rightarrow S_0$	H−1←L (0.68)	396	0.563
3b	402	0.018	$S_1 \rightarrow S_0$	H ← L (0.66)	412	0.021
3c	456	0.083	$S_2 \rightarrow S_0$	H ← L + 1 (0.65)	471	0.117
3d	421	0.107	$S_1 \rightarrow S_0$	H ← L (0.65)	422	0.144
4a	416	0.397	$S_1 \rightarrow S_0$	H ← L (0.62)	453	0.624
4b	404	0.361	$S_1 \rightarrow S_0$	H ← L (0.62)	427	0.536
4c	407	0.241	$S_1 \rightarrow S_0$	H ← L (0.62)	423	0.392
4d	395	0.242	$S_1 \rightarrow S_0$	H ← L (0.63)	401	0.366

H HOMO, *L* LUMO
[a] The values in gas phase
[b] The values in $CHCl_3$

E_g values are found in derivatives **4a**–**4d**, thus their λ_{abs} are more red-shifted than the others. The calculated results at the TD-PBE0/6-31+G(d) level are similar to those at the TD-B3LYP/6-31G(d) level, the maximum deviation is 7 nm for **3a**, the others are only 3 or 4 nm shorter than the TD-B3LYP/6-31G(d) results. Moreover, the same trend of the calculated λ_{abs} values is also obtained from the TD-PBE0/6-31+G(d). In order to show a further explanation of the solvent effect for the H/R substituted derivatives, we predict the absorption spectra in $CHCl_3$ solvent. The introduction of the solvent effect (PCM model) in the TD-B3LYP calculations (Table 4) leads to a red shift for the λ_{abs} values (the PCM results of the TD-PBE0/6-31+G(d) are listed in Table S4 in Supporting Information). The largest red shifts (40–13 nm) are found in $–NO_2$ and push–pull substituted derivatives, the other derivatives with –CN, $–NH_2$, and $–CH_3$ substituents do not show any obvious red shift (only 5–6 nm of red shift). The calculations at the PCM-TD-PBE0/6-31+G(d) level show the similar results to that for the PCM-TD-B3LYP/6-31G(d), the maximum deviation within these two methods is 6 nm.

3.4.2 Emission spectra

The calculated emission parameters at the TD-B3LYP/6-31G(d) level are listed in Table 4, and the results at the TD-PBE0/6-31+G(d) level are listed in Table S4 in Supporting Information. According to Table 4, the emission spectra of the H/R substitution on position 6/6′ are red shifted comparing with **SSF**. Namely, the red-shifted wavelength ($\Delta\lambda_{em}$) is predicted in the increasing order –CN < $–OCH_3$ < $–NO_2$ < $–NH_2$ for the mono-substituted derivatives, and $–NO_2$ < –CN < $–OCH_3$ < $–NH_2$ for the di-substituted series. The $S_1 \rightarrow S_0$ transition corresponds mainly to a LUMO→HOMO excitation. Hence, the trend of the red shift is ascribed to the change of E_g in their S_1 as mentioned in Sect. 3.3. The red shifts observed for **2c**, **2d**, **3c** and **3d** relative to

the others may be due to the electron-donor character of $-OCH_3$ and $-NH_2$, the HOMO level is more affected than the LUMO level upon the electron-donating substitution especially in di-substitution. For **2b** and **3b**, however, the red shifts can be attributed to the enhancement of the whole π-conjugated backbone and the electron-accepting substitution, which makes their E_{HOMO} and E_{LUMO} stabilized at the same time, the E_{LUMO} is more affected than the E_{HOMO} upon the electron-accepting substitution. Within the derivatives **4a–4d**, as in the case of their S_0, the E_{HOMO} is increased, while the E_{LUMO} is decreased. The E_g values become smaller than those of the electron-accepting di-substituted derivatives, while larger than those of the electron-donating di-substituted derivatives. According to our results, not only λ_{em} are red-shifted, but also the emitting f values of the H/R substituted derivatives are greater than that of SSF, implying that push–pull substitution does induce a significant effect on the emission properties. In general, larger oscillator strengths correspond to larger experimental extinction coefficients, which will intensify fluorescent emitting spectrum. Therefore, the approach may give contribution to develop the property of emitting materials. Substitutions with both the electron-donating and electron-accepting substituents will red shift the optical spectra. It is found that, the stronger the electron-donating/accepting abilities are, the larger are $\Delta\lambda_{em}$. Indeed, with the electron-donating/accepting abilities of $-NH_2/-NO_2$, which are stronger than those of $-OCH_3/-CN$, the predicted $\Delta\lambda_{em}$ are found to be larger. The TD-PBE0 results show the same emission properties as the TD-B3LYP ones in the gas phase. Independently on the basis set used, both these two set of results in gas phase (based on the two functionals) are consistent with the increasing red-shift which is induced by the H/R substitution as described above. Thus, one may conclude that the emission properties discussed in this part are method independent. The most obvious differences in λ_{em} values are found in **3b** and **2a** (19 and 13 nm, respectively) with the TD-B3LYP λ_{em} values being found to be larger than the TD-PBE0 ones. For the other derivatives, the calculated difference in λ_{em} is less than 4 nm.

The bulk solvent effects are evaluated by means of the PCM-TD-B3LYP/6-31G(d) and PCM-TD-PBE0/6-31+G(d) methods for the emission spectra in $CHCl_3$ solvent. For the sake of comparison with λ_{em} values in gas phase (TD-B3LYP), the PCM-TD-B3LYP λ_{em} values are also listed in Table 4 (see Table S4 for PCM-TD-PBE0/6-31+G(d) values). These two sets of results (PCM-TD-B3LYP and PCM-TD-PBE0) reveal the same emitting properties. Recall that the same observation was made between the TD-B3LYP and TD-PBE0 (gas phase) results. A careful analysis of our results reveals that each of these derivatives shows a red-shifted wavelength in the polarized $CHCl_3$ solvent. A relatively significant red-shift of 12–37 nm was predicted on the λ_{em} values of derivatives **2a/c**, **3a/c**, and **4a/b/c**, while for **2b/d**, **3b/d**, and **4d**, a substantial solvent effect (λ_{em} variation of less than 10 nm) was predicted, due to their weakly polar properties. Moreover, all the f values in $CHCl_3$ are larger than those in gas phase, implying that the fluorescent emitting spectrum is strengthened in $CHCl_3$ solvent.

3.4.3 Charge transfer analysis

In general, a charge-transfer excited state can be described in molecular orbital terminology, by an excitation between two geometrically distinct parts of the molecule. For the derivatives with push–pull system (**4a**–**4d**), although the orbitals are spread over the whole molecule, the HOMO presents a larger electron density around the donor group, while the LUMO mostly lies on the acceptor part. As recently reported in TD-DFT calculations, the appearance of spurious charge-transfer states (CT states) below the excited state is known to have significant effects on the predicted emission spectra of several push–pull (donor–acceptor) substituted molecules [69]. Thus, we predicted the CT states of the push–pull derivatives using both the TD-B3LYP/6-31G(d) and TD-BH and HLYP/6-31G(d) levels, with the aim to indicate that the CT states in this study are not method dependent. Our results show that both the two methods show an obvious CT state with larger oscillator strengths. It means that these CT states within **4a**–**4d** are not spurious, and the calculated results are method independent. For push–pull systems (**4a**–**4d**), the electrons transfer from pull to push direction in A fragment upon emission process (the map is given in Fig. 5). Electron population change associated with the vertical excitation is investigated through the natural bond orbital (NBO) [70] calculation. The quantitative charge transfer according to the distribution of Mulliken [71] and NBO charge, which are all reliable for describing the quantitative charge transfer,

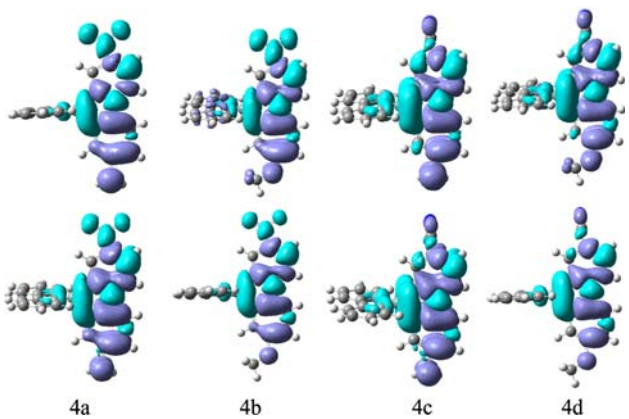

Fig. 5 Charge difference densities of push–pull derivatives in emission. The *upper line* is based on TD-B3LYP, the *lower line* is based on TD-BHandHLYP

Table 5 The quantitative charge transfer of Mulliken and NBO charge (in the parameters) based on the TD-B3LYP/6-31G(d) in excited states

Charge (e^-)	B	C	D	Si
4a	0.012 (0.016)	0.272 (0.296)	−0.362 (−0.374)	0.078 (0.063)
4b	−0.02 (−0.016)	0.248 (0.27)	−0.307 (−0.318)	0.078 (0.063)
4c	0.039 (0.044)	0.12 (0.145)	−0.287 (−0.294)	0.128 (0.105)
4d	0.023 (0.028)	0.092 (0.114)	−0.238 (−0.243)	0.123 (0.101)

C part contains the atoms C'_2, C'_3, C'_4, C'_5, C'_6, C'_7 and –NO_2/–CN, (**4a** and **4b**)/(**4c** and **4d**) D part contains the atoms $C_2, C_3, C_4, C_5, C_6, C_7$ and –NH_2/–OCH_3, (**4a** and **4c**)/(**4b** and **4d**); B is the rest moiety of the spirosilabifluorene

are listed in Table 5. An observation to be noted is that the charge transfer occurs within derivatives **4a**–**4d**, implying that $S_1 \rightarrow S_0$ transitions is an electron transfer from the electron-accepting to the electron-donating groups. Thus, these derivatives lead to charge transfer between different parts, and they may be considered as photoinduced charge transfer materials.

3.5 The effect of the mono-, di-, tri- and tetra- substitutions

With the aim to get an explanation of the effect of the mono-, di-, tri- and tetra-substitution, we extended our theoretical work to include asymmetric mono- (R_1), tri- (R_1, R_2, R_3) and symmetric di- (R_1, R_2), tetra- (R_1, R_2, R_3, R_4) substituted SSF, and determined how the substitution with one, two, three or four aryls (phenyl, biphenyl, pyridyl, and bipyridyl) affects the electronic and optical properties. H/–NH_2 tri- and tetra-substitutions were also considered to confirm whether or not such kinds of substitution can affect their electronic and optical properties. In Table 6, we list the calculated FMO energies, E_g, absorption and emission wavelengths (λ_{abs} and λ_{em}), the oscillator strength (f), and the main CI expansion of these derivatives. For λ_{em} calculation, only some of these derivatives were considered for CIS optimization of the S_1 geometry, due to the limitations of the computational resources for such large systems.

The electron density contours of the FMOs for these derivatives in S_0 and S_1 states are shown in Figure S5 (Supporting Information). The results revealed that the FMOs are mainly distributed on the silafluorene parts and the adjacent aryl rings. The FMOs of the mono-, di- and tri-substituted derivatives are mainly located on A moiety, which contains one (two) phenyl ring(s), while the FMOs of the tetra-substituted derivatives are located on the whole molecules in S_0 due to their higher symmetry, and located on A moiety in S_1 as in the cases of **1a–1d** (Figs. 2 and S1). The bonding–antibonding patterns of their FMOs are similar to those for **1a–1d**. In the cases of ***n*a-*n*d** (n = 5–8), the E_{HOMO} increases and the E_{LUMO} decreases ongoing from mono- to di-aryl substituted derivatives, while from di- to tri- and tetra-aryl substituted derivatives, both the E_{HOMO} and the E_{LUMO} do not change significantly. Thus, the E_g of all the di-, tri- and tetra-substituted derivatives are similar.

According to the results in Table 6, one can also find that the effect of substitutents for optical properties such the λ_{abs} is in the same order as phenyl < biphenyl, pyridyl, and bipyridyl, for each series of mono-, di-, tri-, or tetra-aryl substituted derivatives. Furthermore, each series of di-, tri- and tetra-aryl substituted derivatives possesses similar electronic and optical properties. Taking the mono-, di-, tri- and tetra-substituted derivatives with phenyl ring as examples, the analysis of the optical properties of **5a–5d** indicates that λ_{abs} and λ_{em} of the derivatives with di-, tri- and tetra-aryl substituents do not show any significant difference, only a slight blue shift being found for **5a**. The λ_{abs} and λ_{em} values of **5b**, **5c** and **5d** are nearly identical, which is consistent with the similar E_g. Within the di-, tri- and tetra-substituted derivatives (**5b**, **5c** and **5d**), λ_{abs} or λ_{em} values only vary by less than 3 nm, while f decreases in the order of **5b** > **5c** >**5d** > **5a**. The larger f values for **5b** and **5c** can be explained by the phenyl group, which plays an important role in enhancing f. Both the red shifts and the larger f values can be attributed to the enhanced whole π-conjugated backbone from the other phenyl ring on A fragment. Due to the higher symmetry, f value of **5d** decreases. Such kind of trend can be also found in mono-, di-, tri- and tetra- H/R substituted derivatives (we can take –NH_2 substitution for example). For the tri- and tetra- substituted –NH_2 derivatives, the FMOs are also found to be localized on one of the silafluorene parts. Moreover, both their E_{HOMOs} and E_{LUMOs} decrease slightly, but the E_g do not change too much comparing with the E_g value of the di-substitution, and consequently their absorption and emission spectra.

Therefore, one may conclude that tri- or tetra-substitution does not remarkably affect the electronic and optical properties compared to symmetric di-substitution. It can be confirmed that the maximum changes in the optical properties and electronic structures can be obtained by symmetric di-substituted derivatives.

Table 6 The B3LYP/6-31G(d) and the TD-B3LYP/6-31G(d) computed FMO energies, E_g, wavelengths (λ_{abs} and λ_{em}), oscillator strengths (f) and main CI expansion/coefficient

	λ (nm)	f	Main CI expansion/ coefficient	E_{HOMO} (eV)	E_{LUMO} (eV)	E_g (eV)
Absorption						
5a	310	0.221	H → L (0.64)	−5.70	−1.15	4.55
5b	324	0.522	H → L (0.65)	−5.59	−1.25	4.34
5c	324	0.483	H → L (0.65)	−5.59	−1.26	4.33
5d	327	0.312	H → L (0.67)	−5.57	−1.25	4.31
6a	316	0.504	H → L (0.65)	−5.64	−1.21	4.43
6b	335	1.147	H → L (0.66)	−5.52	−1.33	4.19
6c	336	1.093	H → L (0.66)	−5.52	−1.34	4.19
6d	337	0.833	H → L (0.65)	−5.51	−1.36	4.15
7a	315	0.354	H → L (0.64)	−5.72	−1.30	4.42
7b	335	0.811	H → L (0.65)	−5.61	−1.48	4.13
7c	336	0.712	H → L (0.66)	−5.62	−1.49	4.13
7d	341	0.322	H → L (0.68)	−5.60	−1.52	4.08
8a	316	0.413	H → L (0.55)	−5.72	−1.30	4.42
8b	336	0.946	H → L (0.64)	−5.62	−1.48	4.14
8c	338	0.862	H → L (0.64)	−5.62	−1.49	4.13
8d	341	0.446	H → L (0.67)	−5.61	−1.52	4.09
Tri–NH_2	356	0.035	H → L+1 (0.67)	−4.63	−0.55	4.08
Tetra–NH_2	356	0.025	H → L (0.65)	−4.69	−0.71	3.98
Emission						
5a	381	0.387	H ← L (0.63)	−5.29	−1.64	3.65
5b	404	0.773	H ← L (0.64)	−5.17	−1.74	3.43
5c	404	0.756	H ← L (0.64)	−5.18	−1.75	3.43
5d	405	0.736	H ← L (0.63)	−5.18	−1.75	3.43
Tri–NH_2	441	0.094	H ← L (0.64)	−4.21	−0.87	3.34
Tetra–NH_2	439	0.094	H ← L (0.64)	−4.24	−0.91	3.33

4 Conclusion

Our theoretical results shed light on the electronic and optical properties of a novel class of recently synthesized and characterized spirosilabifluorenes, and predicted the optical properties for a number of newly designed derivatives. The calculated optical results of **1a**–**1d** are in good agreement with experimental results. Both the similar FMO distribution patterns and the similar E_g values for **1a**–**1d** may be responsible for their similar optical data. In general, the E_g of the H/R substituted derivatives are predicted to decrease, confirming a new set of candidates for blue emitting materials. On the basis of the equilibrium geometries, the effect of the substitution on the absorption and emission spectra is evaluated. According to our results, a symmetric di-substitution with –NH_2/–OCH_3 groups and that with push (–NH_2) and pull (–NO_2) groups (on *para*-position) may lead to red shifted (56–96 nm) emission spectra, which could greatly modulate and improve the electronic and optical properties of these spiro-linked derivatives. Furthermore, we find that adding push–pull substituents on one fragment of SSF plays a key role in enlarging the oscillator strength, which will increase the fluorescent intensity. As one may figure out from our results, the maximum change of this system in electronic and optical properties can be obtained from symmetric di-substitution.

Using theoretical methodologies, we show that it is possible to predict reasonable electronic and optical properties of spiro-linked systems, and we are convinced that the systematic use of those theoretical tools should give some hands to efficient syntheses efforts and help to understand more about the structure–properties relation of these materials.

Acknowledgments Financial supports from the NSFC (No. 50473032), NCET-06-0321, and NENU-STB07007 are gratefully acknowledged.

References

1. Tang CW, Van Slyke SA (1987) Appl Phys Lett 51:913
2. Kulkarni AP, Tonzola CJ, Babel A, Jenekhe SA (2004) Chem Mater 16:4556

3. Lee SK, Hwang DH, Jung JB, Cho NS, Lee J, Lee JD, Shim HK (2005) Adv Funct Mater 15:1647
4. Liu J, Zhou QG, Cheng YX, Geng YH, Wang LX, Ma DG, Jing X B, Wang FS (2005) Adv Mater 17:2974
5. Tu GL, Mei CY, Zhou QG, Cheng YX, Geng YH, Wang LX, Ma DG, Jing XB, Wang FS (2006) Adv Funct Mater 16:101
6. Liu J, Zhou QG, Cheng YX, Geng YH, Wang LX, Ma DG, Jing XB, Wang FS (2006) Adv Func Mater 16:957
7. Yang R, Wu H, Cao Y, Ba ZG (2006) J Am Chem Soc 128:14422
8. Jiang J, Xu Y, Yang W, Guan R, Liu Z, Zhen H, Cao Y (2006) Adv Mater 18:1769
9. Wong KT, Chien YY, Chen RT, Wang CF, Lin YT, Chiang HH, Hsieh PY, Wu CC, Chou CH, Su YO, Lee GH, Peng SM (2002) J Am Chem Soc 124:11576
10. Steuber F, Staudigel J, Stössel M, Simmerer J, Winnacker A, Spreitzer H, Weissörtel F, Salbeck J (2000) Adv Mater 12:130
11. Wu CC, Lin YT, Chiang HH, Cho TY, Chen CW, Wong KT, Liao YL, Lee GH, Peng SM (2002) Appl Phys Lett 81:577
12. Schneider D, Rabe T, Riedl T, Dobbertin T, Werner O, Kröger M, Becker E, Johannes HH, Kowalsky W, Weimann T, Wang J, Hinze P, Gerhard A, Stössel P, Vestweber H (2004) Appl Phys Lett 84:4693
13. Saragi TPI, Pudzich R, Fuhrmann T, Salbeck J (2004) Appl Phys Lett 84:2334
14. Bach U, Lupo D, Comte P, Moser JE, Weissörtel F, Salbeck J, Spreitzer H, Grätzel M (1998) Nature 395:583
15. Cabanillas-Gonzalez J, Yeates S, Bradley DDC (2003) Synth Met 139:637
16. Kim SY, Lee M, Boo BH (1998) J Chem Phys 109:2593
17. Tian H, Chen B, Liu PH (2001) Chem Lett 30:990
18. Ghosh P, Shabat D, Kumar S, Sinha SC, Grynszpan F, Li J, Noodleman L, Keinan E (1996) Nature 382:25
19. Murata H, Kafafi ZH, Uchida M (2002) Appl Phys Lett 80:189
20. Palilis LC, Murata H, Uchida M, Kafafi ZH (2003) Organic Electronics 4:113
21. Ohshita J, Lee KH, Hamamoto D, Kunugi Y, Ikadai J, Kwak YW (2004) Chem Lett 33:892
22. Mitschke U, Bauerle P (2001) J Chem Soc Perkin Trans 1:740
23. Wu RL, Schumm JS, Pearson DL, Tour JM (1996) J Org Chem 61:6906
24. Xiao HB, Leng B, Tian H (2005) Polymer 46:5707
25. Pei J, Ni J, Zhou XH, Cao XY, Lai YH (2002) J Org Chem 67:4924
26. Tamao K, Uchida M, Izumizawa T, Furukawa K, Yamaguchi S (1996) J Am Chem Soc 118:11974
27. Yamaguchi S, Endo T, Uchida M, Izumizawa T, Furukawa K, Tamao K (2000) Chem Eur J 6:1683
28. Watkins NJ, Mdkinen AJ, Gao Y, Uchida M, Kafafi ZH (2004) Proc SPIE Int Soc Opt Engr 5214:368
29. Yin SW, Yi YP, Li QX, Yu G, Liu YQ, Shuai ZG (2006) J Phys Chem A 110:7138
30. Murata H, Malliaras GG, Uchida M, Shen Y, Kafafi ZH (2001) Chem Phys Lett 339:161
31. Maslak P, Chopra A, Moylan CR, Wortmann R, Lebus S, Rheingold AL (1996) J Am Chem Soc 118:1471
32. Wu CC, Liu TL, Hung WY, Lin YT, Wong KT, Chen RT, Chen YM, Chien YY (2003) J Am Chem Soc 125:3710
33. Xiao HB, Shen H, Lin YG, Su JH, Tian H (2007) Dyes Pigments 73:224
34. Lee SH, Jang BB, Kafafi ZH (2005) J Am Chem Soc 127:9071
35. Lukeš V, Pálszegir T, Milota F, Sperling J, Kauffmann HF (2006) J Phys Chem A 110:1775
36. Yang GC, Su ZM, Qin CS (2006) J Phys Chem A 110:4817
37. Sun XB, Liu Y, Xu XJ, Yang CH, Yu G, Zhu DB (2005) J Phys Chem B 109:10786
38. Belletête M, Blouin N, Boudreault PT, Leclerc M, Durocher G (2006) J Phys Chem A 110:13696
39. Ortí E, Viruela PM, Viruela R, Effenberger F (2005) J Phys Chem A 109:8724
40. Jacquemin D, Preat J, Wathelet V, Michèle F, Perpète EA (2006) J Am Chem Soc 128:2072
41. Belletête M, Morin JF, Leclerc M, Durocher G (2005) J Phys Chem A 109:6953
42. Wu C, Tretiak S, Chernyak VY (2007) Chem Phys Lett 433:305
43. Masunov A, Tretiak S (2004) J Chem Phys B 108:899
44. Hariharan PC, Pople JA (1974) Mol Phys 27:209
45. Gordon MS (1980) Chem Phys Lett 76:163
46. Frisch MJ, Pople JA, Binkley JS (1984) J Chem Phys 80:3265
47. Foresman JB, Head-Gordon M, Pople JA, Frisch MJ (1992) J Phys Chem 96:135
48. Becke AB (1993) J Chem Phys 98:5648
49. Lee C, Yang W, Parr RG (1988) Phys Rev B 37:785
50. Stephens PJ, Devlin FJ, Chabalowski CF, Frisch M (1994) J Phys Chem 98:11623
51. Foresman JB, Head-Gordon M, Pople JA, Frish MJ (1992) J Phys Chem 96:135
52. Stratman RE, Scuseria GE, Frisch MJ (1998) J Chem Phys 109:8218
53. Bacon AD, Zerner MC (1979) Theor Chim Acta 53:21
54. Adamo C, Barone V (1999) J Chem Phys 110:6158
55. Clark T, Chandrasekhar J, Spitznagel GW, Schleyer PvR (1983) J Comp Chem 4:294
56. Cancès E, Mennucci B, Tomasi J (1997) J Chem Phys 107:3032
57. Cornard JP, Lapouge C (2006) J Phys Chem A 110:7159
58. Cossi M, Barone V (2001) J Chem Phys 115:4708
59. Becke AD (1993) J Chem Phys 98:1372
60. Gaussian 03, Revision B.03 (2003) Gaussian, Pittsburgh
61. Gaussview 3.0 Reference (2003) Gaussian, Wallingford
62. Stephan Portmann (2002) CSCS/ETHZ http://www.cscs.ch/molekel
63. Marcos AD, Duarte HA, Pernaut JM, Wagner BD (2000) J Phys Chem A 104:8256
64. Halls MD, Schlegel HB (2001) Chem Mater 13:2632
65. Foresman JB, Schlegel HB (1933) In: Gausto R, Hollas JM (eds) Recent experimental and computational advances in molecular spectroscopy, vol 406. Kluwer, Dordrecht, p 11
66. Tirapattur S, Belletête M, Leclerc M, Durocher G (2003) TheoChem 625:141
67. Zhang JP, Frenking G (2004) J Phys Chem A 108:10269
68. Hu B, Gahungu G, Zhang JP (2007) J Phys Chem A 111:4965
69. Magyar RJ, Tretiak S (2007) J Chem Theory Comput 3:976
70. Reed AE, Weinhold F (1983) J Chem Phys 78:4066
71. Mulliken RS (1955) J Chem Phys 23:1833